Smaller is less stable: Size effects on twinning vs. transformation of reverted austenite in TRIP-maraging steels

M-M. Wang, C.C. Tasan *, D. Ponge, A. Kostka, D. Raabe

Max-Planck-Institut für Eisenforschung, Max-Planck-Straße 1, 40237 Düsseldorf, Germany

Abstract

Steels containing reverted nanoscale austenite (γ_{RN}) islands or films dispersed in a martensitic matrix show excellent strength, ductility and toughness. The underlying microstructural mechanisms responsible for these improvements are not yet understood, but are observed to be strongly connected to the γ_{RN} island or film size. Two main micromechanical effects are conceivable in this context, namely: (i) interaction of γ_{RN} with microcracks from the matrix (crack blunting or arresting); and (ii) deformation-induced phase transformation of γ_{RN} to martensite (TRIP effect). The focus here is on the latter phenomenon. To investigate size effects on γ_{RN} transformation independent of other factors that can influence austenite stability (composition, crystallographic orientation, defect density, surrounding phase, etc.), a model (TRIP-maraging steel) microstructure is designed with support from diffusion simulations (using DICTRA software) to have the same, homogeneous chemical composition in all γ_{RN} grains. Characterization is conducted by *in-situ* tension and bending experiments in conjunction with high-resolution electron backscatter diffraction mapping and scanning electron microscopy imaging, as well as *post-mortem* transmission electron microscopy and synchrotron X-ray diffraction analysis. Results reveal an unexpected "smaller is less stable" effect due to the size-dependent competition between mechanical twinning and deformation-induced phase transformation.

1. Introduction

Transformation-induced plasticity (TRIP) effects have been observed in many alloys, including TRIP steels [1–4], medium-manganese steels [5], 9% Ni cryogenic steels [6], and quenching and partitioning steels [7,8]. Recently a new alloy system of TRIP-maraging steels, which also benefits simultaneously from the maraging effect, has been added to this list [9,10]. A single aging step sets the basis for these two effects, triggering the partial formation of the reverted nanoscale austenite (γ_{RN}) grains, and the formation of intermetallic nanoprecipitates within the martensite matrix. This enables a wide range of microstructures to be accessible by straightforward thermal processing, and leads to joint increases in both strength and ductility [11]. The TRIP-maraging approach thus creates an attractive pathway for one of the grand challenges in steel design, i.e. increasing ductility and toughness of martensitic steels without sacrificing strength [12].

In this work, we focus on the micromechanical role of size effects on the observed improvements, motivated by our previous analysis showing that the TRIP-induced ductilization is strongly γ_{RN} size dependent [13]. Aside from a few works [14–16], the majority of reports on the stability of metastable austenite focus on size regimes larger than the nanoscale γ_{RN} sizes present in TRIP-maraging steels (i.e. $> \sim 200$ nm in previous works) [3,17–21]. Thus,

* Corresponding author.
  E-mail addresses: c.tasan@mpie.de, c.tasan@tue.nl (C.C. Tasan).

such a micromechanical understanding of the transformation size effects is critical for all nanoscale austenite-containing steels, especially in providing guidelines to fine-tune microstructures to activate the phase transformation over the whole deformation regime [22,23].

Understanding and controlling austenite stability has long remained a key issue in the literature for the design of TRIP-assisted alloys. Previous reports underline the complexity of the problem arising due to a wide variety of different microstructural parameters (grain size [24–27] crystallographic orientation [28,29], chemical composition [25,30,31], etc.). Additional micromechanical complexity is introduced due to strong strain partitioning and stress shielding effects [20,32] that are intrinsically present in conventional multiphase TRIP steels with hard phases surrounding the austenite. The analysis of transformation size effects of γ_{RN} in TRIP-maraging steels creates an additional advantage to overcome these otherwise complex boundary conditions. As will be shown in detail in the next section, by using carefully designed heat treatments, this alloy provides model microstructures for investigating transformation size effects independent of the aforementioned factors, reducing the complexity of the micromechanical problem mentioned above.

Due to the complexity of the related microstructures and the small length scales involved, a further improvement in the understanding also requires optimization in the experimental methodology employed. The two most commonly used techniques, X-ray diffraction (XRD) and transmission electron microscopy (TEM), even when used *in situ* during deformation, provide either good statistics, but no direct microstructural observation (XRD), or direct microstructural observation, but with limited statistics (TEM). Recently the emerging *in-situ* high-resolution electron backscatter diffraction (HR-EBSD) mapping technique provides an excellent combination of statistics and direct observation of transformation mechanisms [33], and is therefore employed in this work. The data are accompanied by corresponding *post-mortem* analyses conducted with EBSD, TEM and synchrotron X-ray diffraction techniques.

In what follows, first the details of the employed experimental methodology are presented, which also includes the design strategy of the model TRIP-maraging steel microstructure. The results of the *in-situ* and *post-mortem* analyses are then shown and discussed, and finally the conclusions are presented.

2. Experimental procedure

2.1. Model microstructure design

A Fe–9Mn–3Ni–1.4Al–0.01C (mass%) TRIP-maraging steel was cast and hot rolled at 1100 °C. It was homogenized at 1100 °C for 1 h and quenched to room temperature. Partial reversion of martensite back into austenite can be achieved by further annealing. Optimal reversion
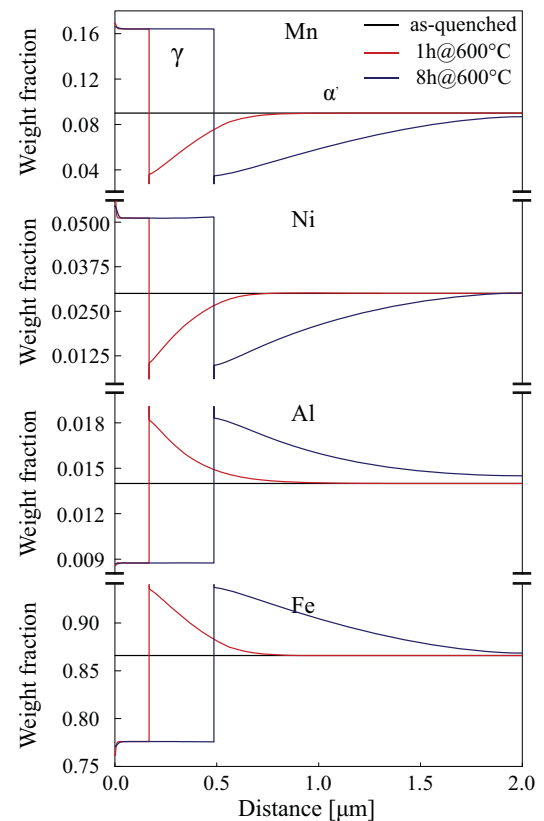

Fig. 1. Predicted reversion of α' martensite back into γ_{RN} in the current Fe–9Mn–3Ni–1.4Al–0.01C (mass%) TRIP-maraging steel at 600 °C for 1 and 8 h, and the corresponding elemental partition of Mn/Ni/Al/Fe, simulated by DICTRA.

conditions were simulated using DICTRA [34]. Two constraints were used as design guidelines: (i) the elemental partitioning had to be controlled to exclude compositional effects on phase stability; (ii) growth kinetics of the reversed austenite had to be optimized to ensure that the γ_{RN} phase could be detected by EBSD, i.e. phase dimensions had to be larger than ~50–80 nm. For these calculations the TCFE7 and MOBFE2 databases were used [35]. As a non-equilibrium phase, kinetic parameters of martensite are not included in the databases. Following previous reports of a similar alloy system [10], martensite was thus thermodynamically and kinetically treated as ferrite, but with increased elemental diffusivity. As boundary condition, an inactive austenite layer[1] (γ) with a planar interface was attached to the left side of a martensite phase (α' martensite) with a 2 μm cell size (Fig. 1). From these simulations an optimal reversion temperature of 600 °C was determined and the reversion process was calculated up to 100,000 s. Following these simulation results, annealing of the samples was also carried out at 600 °C for various periods (1, 4 and 8 h).

---

[1] An "inactive phase" does not participate in the simulation until it becomes stable. As we start from single martensite phase and austenite will be formed as a new phase during reversion, it is treated here initially as inactive phase.

2.2. Microstructure characterization

The microstructure evolutions due to the (600 °C 1/4/8 h) reversion treatments and subsequent deformation experiments were investigated in detail. To induce deformation, two types of experiments were carried out: (i) room temperature uniaxial tensile tests of dog-bone samples conducted at a strain rate of $10^{-3}\,\text{s}^{-1}$ using a Kammrath and Weiss tensile stage; and (ii) *in-situ* SEM three-point bending experiments. Samples for *post-mortem* microstructure characterization were analyzed during the deformation using digital image correlation analysis (Aramis software, GOM GmbH), to determine local strain levels [36,37].

To characterize the microstructures, SE imaging, energy-dispersive X-ray spectroscopy (EDX), HR-EBSD, TEM and synchrotron X-ray diffraction techniques were employed. HR-EBSD was used for the analysis of γ_{RN} after reversion and during deformation. Samples for SEM analysis were prepared by grinding, polishing in diamond suspension and final polishing in colloidal silica suspension. The last step ensures a deformation-free surface. HR-EBSD measurements were performed using a JEOL JSM-6500F field emission gun scanning electron microscope equipped with a high-speed CCD camera for pattern recording, and analyzed by TSL-OIM software. The samples were positioned with the surface normal tilted at 70° with respect to the incident beam towards the EBSD detector. Measurements were carried out at 15 kV at a step size of 80 nm. In relevant regions, EDX measurements were also carried out to reveal elemental partitioning between α' martensite phase and γ phase. For EBSD observation during *in-situ* tensile testing, the same area was tracked after each deformation step. In the case of *post-mortem* testing, samples deformed to different strain levels were prepared following conventional sample preparation procedures and then probed by EBSD. EBSD sample preparation and microstructure measurements in the course of the deformation experiments are shown in Fig. 3.

TEM studies were applied to reveal deformation mechanisms of the 600 °C 8 h sample. Specimens for TEM analysis were prepared from 3 mm disks of tensile samples. The discs were ground to ~100 μm thickness and then thinned using the Tenupol 5 double-jet electropolishing system (electrolyte: 10% perchloric acid and 90% methanol; temperature −32 °C; voltage: 16 V). TEM observations were performed in JEOL JEM-2200FS operated at 200 kV.

Synchrotron X-ray diffraction was applied for observing phase transformations during deformation. The measurements were performed at the high-resolution powder diffraction beamline P02.1 at PETRA III (DESY Hamburg, Germany) using a wavelength of $\lambda = 0.20727$ Å. An incident beam with dimensions of $200 \times 200\ \mu\text{m}^2$ was used. After penetrating a 1 mm thick sample with known pre-strain values, the two-dimensional XRD patterns were collected using a Perkin Elmer 1621 fast image plate detector (2048×2048 pixels, $200 \times 200\ \mu\text{m}^2$ pixel size, intensity resolution of 16 bit), which was placed at a distance of 800 mm from the sample. XRD patterns were integrated into 2θ-space using the software FIT2D [38], and then analyzed by the Rietveld method in MAUD [39].

3. Results

3.1. Model microstructure design

The DICTRA simulations of the reverse transformation of α' martensite back into γ_{RN} in the current Fe–9Mn–3Ni–1.4Al–0.01C (mass%) TRIP-maraging steel are shown in Fig. 1. Here, the growth of γ_{RN} from α' martensite, and the accompanying elemental partitioning of Mn/Ni/Al/Fe after 1 and 8 h annealing, respectively, at 600 °C are presented. After being subjected to 600 °C annealing for 1 h, γ_{RN} grows with uniform chemical composition to ~100 nm thickness. With increasing the annealing time to 8 h, γ_{RN} grains continue to grow but maintain the same chemical composition. Thus, to be able to produce γ_{RN} with no compositional gradients and at size scales measurable by EBSD, aging treatments can be carried at 600 °C for times longer than 1 h.

Next, the thus-determined annealing treatment is applied to the Fe–9Mn–3Ni–1.4Al–0.01C (mass%) alloy. Prior to the reversion treatment, the TRIP-maraging steel microstructure consists of a single α' martensite phase with a homogeneous distribution of Mn, Ni, Al and Fe (Fig. 2a). No microsegregation or retained γ was detected within the resolution limits of EDX and HR-EBSD. After 600 °C 1 h annealing, a thin layer of γ_{RN} grows along the prior γ grain boundaries and α' martensite packet/block boundaries (Fig. 2b). After 8 h further annealing, all α' martensite lath boundaries are decorated by γ_{RN} grains (Fig. 2c). Comparison of the 2-D sections of the resulting microstructures in Fig. 2b and c reveals that the period of the annealing treatment has a direct influence on the continuity of the γ_{RN} grain network and thus also on the 3-D morphology of γ_{RN} grains. The extended annealing treatment leads to a quasi-continuous γ_{RN} network that decorates all martensitic boundaries with only limited gaps in between. In 3-D, the austenite grains are films that follow the complex 3-D boundary network of lath martensite [40], with slight variations in thickness. Confirming the calculations by DICTRA, γ_{RN} assumes a uniform chemical composition, e.g. as shown in Fig. 2c (by SEM-EDX analysis) and as shown in the inset in Fig. 2c$_1$ (by TEM-EDX analysis). No obvious partition of Ni between α' martensite and γ_{RN} was detected by EDX.

Thus, the predicted microstructures are experimentally confirmed by EBSD and EDX to contain γ_{RN} grains with homogeneous chemical composition. This point is essential in order not to confuse purely size-dependent TRIP effects (such as targeted here) with composition-dependent phenomena, i.e. with a situation where different austenite grains may also have different chemical composition. As shown by the inverse pole figure (IPF) in Fig. 2d, all γ_{RN} grains formed from the same α' martensite blocks, such
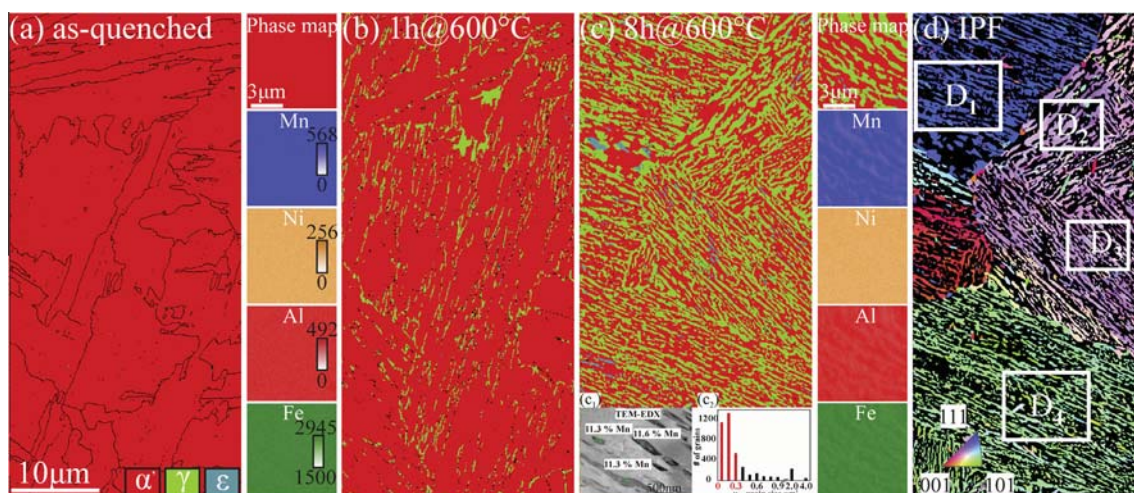
Fig. 2. (Color online) Microstructure evolution due to the reversion treatment characterized by HR-EBSD and EDX: (a) quenched state; (b) 600 °C, 1 h sample; (c) 600 °C, 8 h sample; (d) inverse pole figure map (IPF) of γ_{RN} grains in the same area as (c). Each EDX map is color coded by the count frequency of corresponding X-ray signal received by the EDX detector. EDX measurements of γ_{RN} grains from TEM are shown as an inset in Fig. 2c$_1$. The area distribution of γ_{RN} grains is shown as an inset in Fig. 2c$_2$. This area distribution of the undeformed state is compared in Fig. 6a to that of different deformed states.

as, for example, visible in regions D_1, D_2 and D_4, exhibit the same crystallographic orientation. Hence, through the application of a simple heat treatment (600 °C, 8 h), optimized microstructures for studying the grain size dependence of the TRIP effect, independent of chemical composition, crystallographic orientation, geometric orientation and influence of second phase and defect structure (Fig. 7) are achieved.[2] Thus, all the following mechanical tests were carried out on 600 °C 8 h sample with the optimized γ_{RN} grain size.

3.2. Deformation-induced microstructure evolution

Fig. 3 shows the evolution of the γ_{RN} fraction (green data points) and also of the ε-martensite fraction (blue data points) during the tensile tests as measured by *in-situ* (square) and *post-mortem* (triangle) EBSD. The phase maps obtained from these measurements are given in Fig. 4. As shown in the inset, the *in-situ* data points are measured from the surface of a deforming sample, while the *post-mortem* measurements are obtained from the bulk. The EBSD quantification reveals good correspondence with the XRD measurements, carried out both in the undeformed state (XRD, green cross data point) and in the severely deformed state (synchrotron X-ray diffraction, green plus data point). Both sets of independent data taken from *in-situ* (i.e. surface) and *post-mortem* (i.e. bulk) EBSD analyses reveal that the γ_{RN} fraction decreases over the entire deformation process. This decrease is more drastic at the early stage of deformation
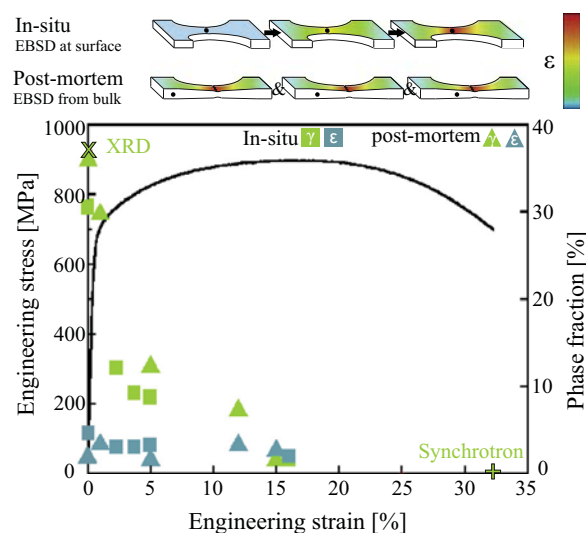

Fig. 3. Evolution of phase fraction (γ_{RN} in green, ε-martensite in blue) in the 600 °C, 8 h sample during *in-situ* (square data points) and *post-mortem* (triangular data points) tensile tests measured by HR-EBSD. Green cross and plus data points represent the γ_{RN} fraction measured by XRD in the undeformed state and synchrotron X-ray diffraction measurements obtained in the deformed state, respectively. All other data points were taken by EBSD. (For interpretation of the references to color in this figure legend, the reader is referred to the web version of this article.)

(around ε = 3%) compared to the lower transformation rate at the later stage of deformation. The fraction of ε-martensite remains almost constant over the entire deformation regime. Comparison of the two data sets (i.e. surface vs. bulk) reveals that the influence of possible surface effects (i.e. due to the evolving roughness, difference in stress state, etc.) do not have a significant effect on the overall trend that is observed.

---

[2] This microstructure also allows us to study crystallographic or geometric effects, e.g. D_1 vs. D_4 or D_2 vs. D_3, respectively. Geometric orientation means the geometric alignment of grains with respect to the loading direction.
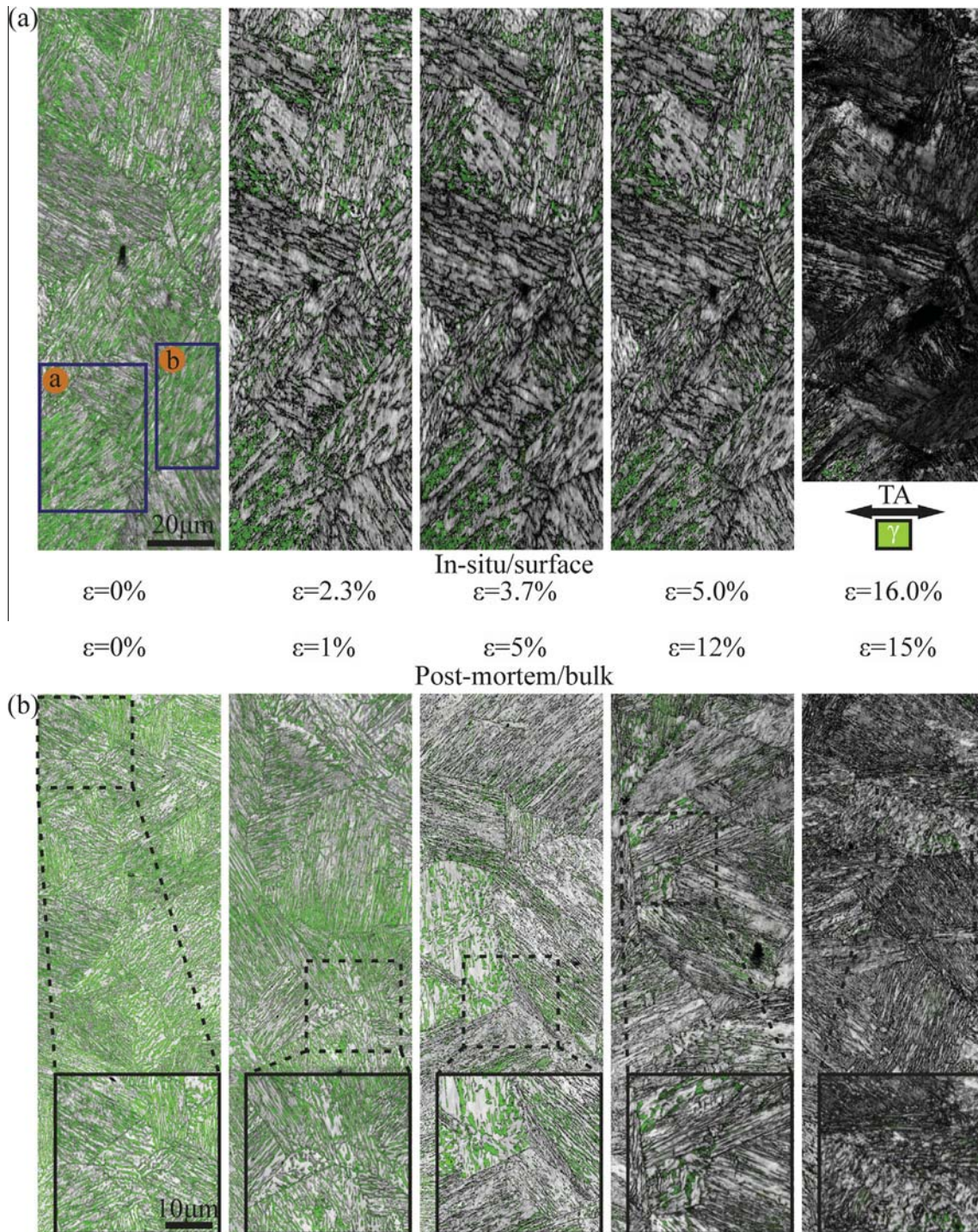
Fig. 4. (Color online) Evolution of γ_{RN} phase during (a) *in-situ* (surface data probed) and (b) *post-mortem* (bulk data probed) tensile tests. For the *in-situ* data set, two areas, a and b, are outlined and will be further analyzed in Fig. 5. For the *post-mortem* data set, a magnified image is inserted for each map (TA, tensile axis).

The characteristics and trends of the γ_{RN} transformation can be studied from the phase maps obtained during *in-situ* and *post-mortem* tensile tests shown in Fig. 4a and b, respectively. Here, each map is an overlay of the corresponding EBSD image quality map (in greyscale) and the γ_{RN} phase map (in green). For the *post-mortem* measurements (probing different areas deformed to different strain levels), a magnified image was inserted for each map for a more detailed analysis of the influence of size effects on γ_{RN} stability.

The γ_{RN} grains have various sizes in the undeformed state (Fig. 4), as is already shown in the phase maps after the aging treatment (Fig. 2c). According to the γ_{RN} grain size distribution shown in Fig. 2c$_2$, the majority of γ_{RN}

grains (>72% number fraction) are smaller (with grain size from 0.1 to 0.3 μm^2), and the other γ_{RN} grains (~28% number fraction) are relatively larger (with grain size from 0.3 to 4.0 μm^2). These dimensions are also confirmed with higher-resolution EBSD measurements (30 nm step size) and SEM backscatter electron and TEM bright-field analyses (not shown here). Hence, γ_{RN} grains are classified here into two groups according to their grain size, namely group I (0.1–0.3 μm^2) and group II (0.3–4 μm^2). After straining to $\varepsilon = 2.3\%$, most of the γ_{RN} grains in group I (~58%, as will later be shown in Fig. 6), i.e. with small grain sizes, have already transformed into α' martensite, while the majority of the γ_{RN} grains belonging to group II (~63%, as will later be shown in Fig. 6), i.e. with larger grain sizes, remain untransformed in the microstructure. These larger γ_{RN} grains in group II show higher resistance to phase transformation and remain untransformed until $\varepsilon = 5.0\%$. With further straining to $\varepsilon = 16.0\%$, the evolving surface morphology leads to poor image quality and difficulty in the EBSD measurements. Even then, 0.06% of the larger γ_{RN} grains pertaining to group II still remain untransformed, unexpectedly indicating higher phase stability against deformation-stimulated transformation. These observations on the transformation size effect, namely the higher resistance of the larger γ_{RN} grains (group II: 0.3–4 μm^2) to deformation-driven transformation compared to that of the smaller γ_{RN} grains (group I: 0.1–0.3 μm^2), are consistent within the behavior of each of the γ_{RN} colonies in Fig. 4. Moreover, comparisons between different γ_{RN} colonies (i.e. within different α' martensite blocks) also underline the different relative transformation rates due to crystallographic orientation effects on the mechanical stability.

This unexpected "inverse" size effect of the γ_{RN} stability, i.e. the fact that a smaller γ_{RN} grain size does not contribute to a higher phase stability to transformation, is confirmed also by *post-mortem* measurements. In order to exclude the influence of evolving surface morphology during *in-situ* deformation, *post-mortem* tensile tests and follow-up EBSD measurements are conducted. These measurements are carried out on several samples pre-deformed to different strain levels and repolished after deformation, i.e. inside the bulk material of the pre-deformed samples. As shown by the magnified images taken for increasing strain levels in Fig. 4, the majority of the larger γ_{RN} grains (group II: 0.3–4 μm^2) remains untransformed up to high strain levels, again also depending on the crystallographic orientation of the γ_{RN} grains.

Two areas, a and b, outlined in the *in-situ* data set, are analyzed in more detail in order to obtain an understanding of the origin of this unexpected inverse transformation size effect (i.e. "smaller is less stable"). More specifically, we aim at understanding the microstructural features that control the γ_{RN} stability (Fig. 5). It needs to be taken into account that the γ_{RN} grains in these two areas have different crystallographic orientations, as shown by the IPF map of the γ_{RN} grains with respect to the tensile axis (TA). For

area a, in addition to the phase map, image quality (IQ) and kernel average misorientation (KAM) maps of γ_{RN} are also shown (Fig. 5a). The KAM is the average local misorientation of all neighboring points (here to the second nearest pixel) to a given measurement point. This accumulated lattice curvature value is used as an indirect measure to represent the local defect density in the γ_{RN} grains [41,42]. In order to eliminate the undesired contributions of EBSD data pixels that stem from the α' martensite phase or from the immediate vicinity of the α' martensite/γ_{RN} phase boundaries, misorientations above 2° are discarded from the calculation. This means that we use the KAM measure here only to quantify the generic defect density that is stored inside the γ_{RN} grains. In addition to the γ_{RN} and α' martensite phases, the thermally induced ε-martensite is also observed in the undeformed state.[3]

As shown in Fig. 5a, the γ_{RN} grains that are formed between the α' martensite lath variants consist of smaller grains (group I: 0.1–0.3 μm^2) and larger grains (group II: 0.3–4 μm^2) prior to deformation. In order to elucidate the transformation size effects, the γ_{RN} grains belonging to group I and group II are marked individually by either white solid arrows or white open arrows. When comparing these data to Fig. 4, the magnified maps more clearly demonstrate that up to a nominal deformation of $\varepsilon = 2.3\%$, the local strain is preferentially partitioned to the smaller γ_{RN} grains indicated by white solid arrows (group I: 0.1–0.3 μm^2), which transform to α' martensite (phase in red) at these low strain values. Larger γ_{RN} grains marked by the white open arrows (group II: 0.3–4 μm^2), however, remain untransformed, and also appear not significantly plastically deformed. This is concluded from the fact that no significant changes are observed at this strain level in the intrinsic KAM values of these remaining grains. Increased deformation to a nominal strain of $\varepsilon = 3.7\%$ still causes a limited decrease in the overall γ_{RN} fraction of the larger grains (group II: 0.3–4 μm^2), yet leads to a gradual increase in their intrinsic KAM values. Upon deformation to a nominal strain of $\varepsilon = 5.0\%$, these larger γ_{RN} grains (group II: 0.3–4 μm^2) still show only partial transformation into α' martensite and a negligible reduction in grain size, but they do reveal a continued gradual increase in their intrinsic KAM values. When samples are further deformed to a nominal value of $\varepsilon = 16.0\%$, only few of the larger γ_{RN} grains (group II: 0.3–4 μm^2) with high intrinsic KAM value can still be detected by the EBSD measurements.

Aside from using the intrinsic KAM values as a measure for the in-grain deformation, the grain average misorientation (GAM) values of these three larger γ_{RN} grains, are additionally presented in Fig. 6b to confirm the aforementioned

---

[3] Alternative (electropolishing-based) sample preparation and the high confidence index (CI) value of ε-martensite data points (CI > 0.1) confirm that ε-martensite is present in the microstructure after quenching from austenite reversion treatment, and is not due to improper sample preparation or to incorrectly indexed EBSD data points near phase boundaries.
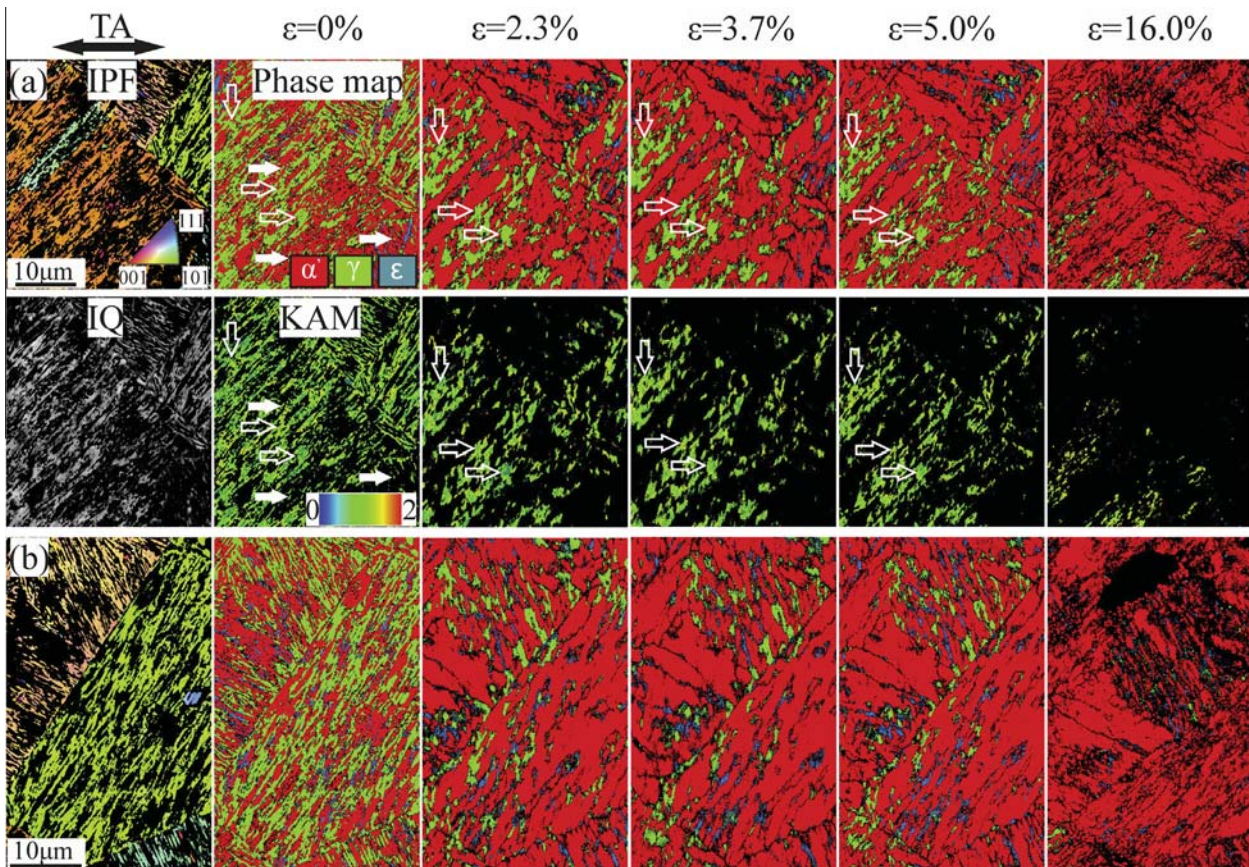
Fig. 5. High-magnification *in-situ* images of the deformation sequence of two outlined areas (a) and (b) in Fig. 4a. EBSD phase maps and inverse pole figure (IPF) with respect to tensile axis (TA) are provided for both areas. For area (a), the image quality (IQ) and KAM maps are also provided.

strain accommodation process of larger γ_{RN} grains (group II: 0.3–4 μm^2). GAM is the misorientation between each neighboring pair of points within the grain. At the early stage of deformation (white area in Fig. 6b), i.e. up to 2.3% strain, larger γ_{RN} grains exhibit a slight increase of the GAM value and pronounced strain accommodation via deformation (blue area in Fig. 6b) only occurs at higher strains, i.e. above 2.3%.

These results suggest that the smaller γ_{RN} grains (group I: 0.1–0.3 μm^2) directly transform into α' martensite after 2.3% strain. In contrast, the larger γ_{RN} grains (group II: 0.3–4 μm^2), at first undergo plastic deformation (between 0% and 2.3% strain) and only after larger deformation (between 2.3% and 16% strain) gradual phase transformation. Careful examination of area b also demonstrates that an analogous transformation size effect is present in this case, despite the different crystallographic orientations of the γ_{RN} grains.

While different phase transformation behaviors can already be observed from the phase evolution presented in Figs. 4 and 5, the transformation size effect of the γ_{RN} grains is further quantified and shown in Fig. 6a and c. The evolution of the number of γ_{RN} grains within different grain size groups during deformation is shown in Fig. 6a. While smaller γ_{RN} grains in group I (with grain size from 0.1 to 0.3 μm^2) account for majority of γ_{RN} grains in the

undeformed state ($\geqslant 72\%$ number fraction), a more drastic reduction in their number is observed upon straining to 2.3%, compared to the larger γ_{RN} grains in group II (with grain size from 0.3 to 4.0 μm^2). The difference in the transformation rate of group I and group II γ_{RN} grains is more clearly observed in Fig. 6c where the combined fractions of untransformed γ_{RN} grains in each grain size group are plotted as a function of the applied strain level. While each grain size group shows gradual transformation behavior of γ_{RN} to α' martensite over the entire deformation process, the small grains (group I) transform faster than the large grains (group II).[4] This is in accordance with the phase evolution presented in Figs. 4 and 5, where smaller γ_{RN} grains transform faster and larger γ_{RN} grains show more reluctance to undergo phase transformation.

In order to understand the deformation mechanisms and phase transformation behavior of the present TRIP-maraging steel, samples prior to deformation and samples deformed to different strain levels, i.e. with 2% and 7% global strain, are also studied by TEM analysis (Fig. 7). Here, for each strain level, STEM and TEM

---

[4] Note that the partial transformation of the γ_{RN} with larger grain size leads to the grain size reduction and therefore results in the overestimation of the count of γ_{RN} with smaller grains. In other words, the size effect is even more pronounced than shown here.
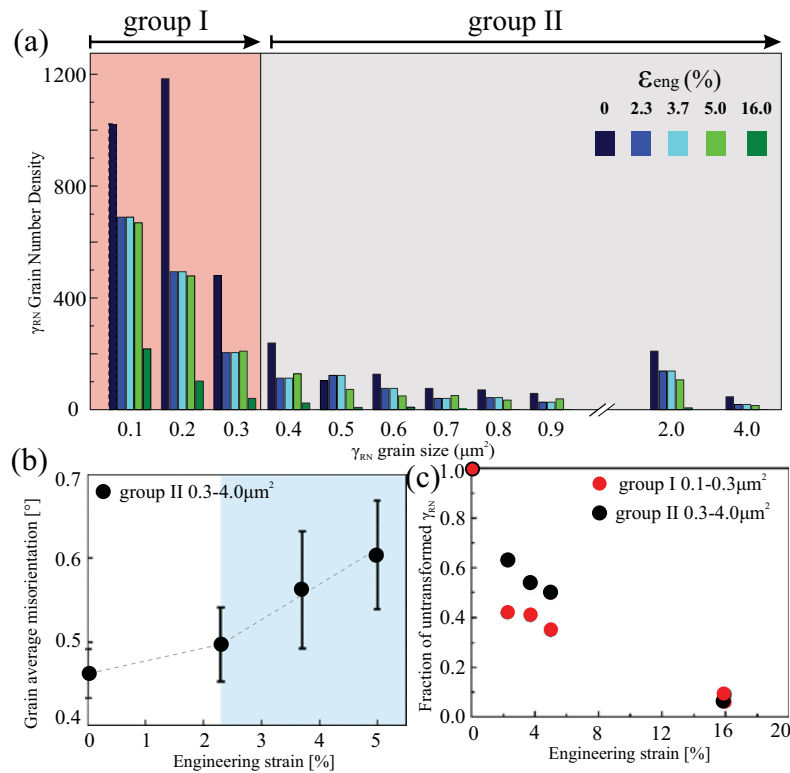
Fig. 6. (a) Evolution of the number of γ_{RN} grains within different grain size groups during deformation. (b) Deformation behavior of larger (group II) γ_{RN} grains revealed by grain average misorientation (GAM) evolution in the three grains indicated by white open arrows in Fig. 5a. Smaller (group I) γ_{RN} grains are too small to form in-grain deformation substructures, and thus no GAM is shown for these. (c) Quantitative analysis of fraction of untransformed γ_{RN} during *in-situ* tension for smaller (group I) and larger (group II) γ_{RN} grains.

analyses of specific areas are presented, together with corresponding diffraction patterns.

The undeformed microstructure consists of an α' martensite matrix with nanoprecipitates and precipitate-free γ_{RN} grains (Fig. 7a). As revealed by bright-field TEM images (Fig. 7a₂), the α' martensite assumes a body-centered cubic (bcc) lattice structure and still contains a high density of dislocations after 8 h at 600 °C. γ_{RN} grains, however, exhibit minor stacking faults (SFs) and do not inherit the defect structure from α' martensite (Fig. 7a₃). When considering this non-inherited defect structure of γ_{RN} grains in conjunction with the accompanying elemental partitioning between α' martensite and γ_{RN} (Fig. 2), the reversion process at isothermal holding at 600 °C is most likely controlled by a reconstructive phase transformation.

With a global strain of 2%, SFs are introduced as a result of motion of partial dislocations in smaller γ_{RN} grains, e.g. the γ_{RN} grain in Fig. 7b₂. The γ_{RN} grains can be distinguished from the α' martensite matrix as they are precipitate free. In most of these investigated areas at this strain level, smaller γ_{RN} grains, e.g. the γ_{RN} grain in Fig. 7b₃, are already transformed into α' martensite. These observations, where smaller γ_{RN} grains are readily transformed to α' martensite at small strains, match the previously presented EBSD results (Figs. 4–6). In contrast, a significant number of boundaries are observed in the larger γ_{RN} grains, as shown by the red and green rectangles in

Fig. 7b₁ and also in the magnified images in Fig 7d₁. These internal interfaces divide the larger crystals into distinct sub-grains, which exhibit different contrast due to their different mutual orientations. This means that up to ~2% strain, larger γ_{RN} grains accommodate deformation by formation of internal boundaries and the development of SFs inside individual sub-grains.

The deformation microstructures further develop as the samples are globally strained to 7%. Smaller γ_{RN} grains, as shown in Fig. 7c₁, show uniform contrast due to the collective transformation to α' martensite. Larger γ_{RN} grains, in contrast, further split into sets of misoriented sub-grains during ongoing straining, as displayed in Fig. 7d₁ (magnified image of Fig. 7c₁), c₂ and 7c₃, in terms of the non-uniform in-grain contrast. To understand the nature of the deformation-induced boundaries and the cause of the observed difference in in-grain contrast, selected-area diffraction analyses were carried out for the regions shown in Fig. 7c₂ and c₃. The corresponding diffraction patterns are reconstructed and presented in Fig. 7d₂ and d₃, respectively.

The γ_{RN} grain shown in Fig. 7c₂ exhibits a complex diffraction spectrum, consisting of γ_{RN} spots plus streaks, as well as ε-martensite and γ_{RN} deformation twin spots (Fig. 7d₂). This observation, hence, strongly suggests that the observed straight boundary with bright contrast in Fig. 7c₂ is a nanotwin. The dark-field image taken in
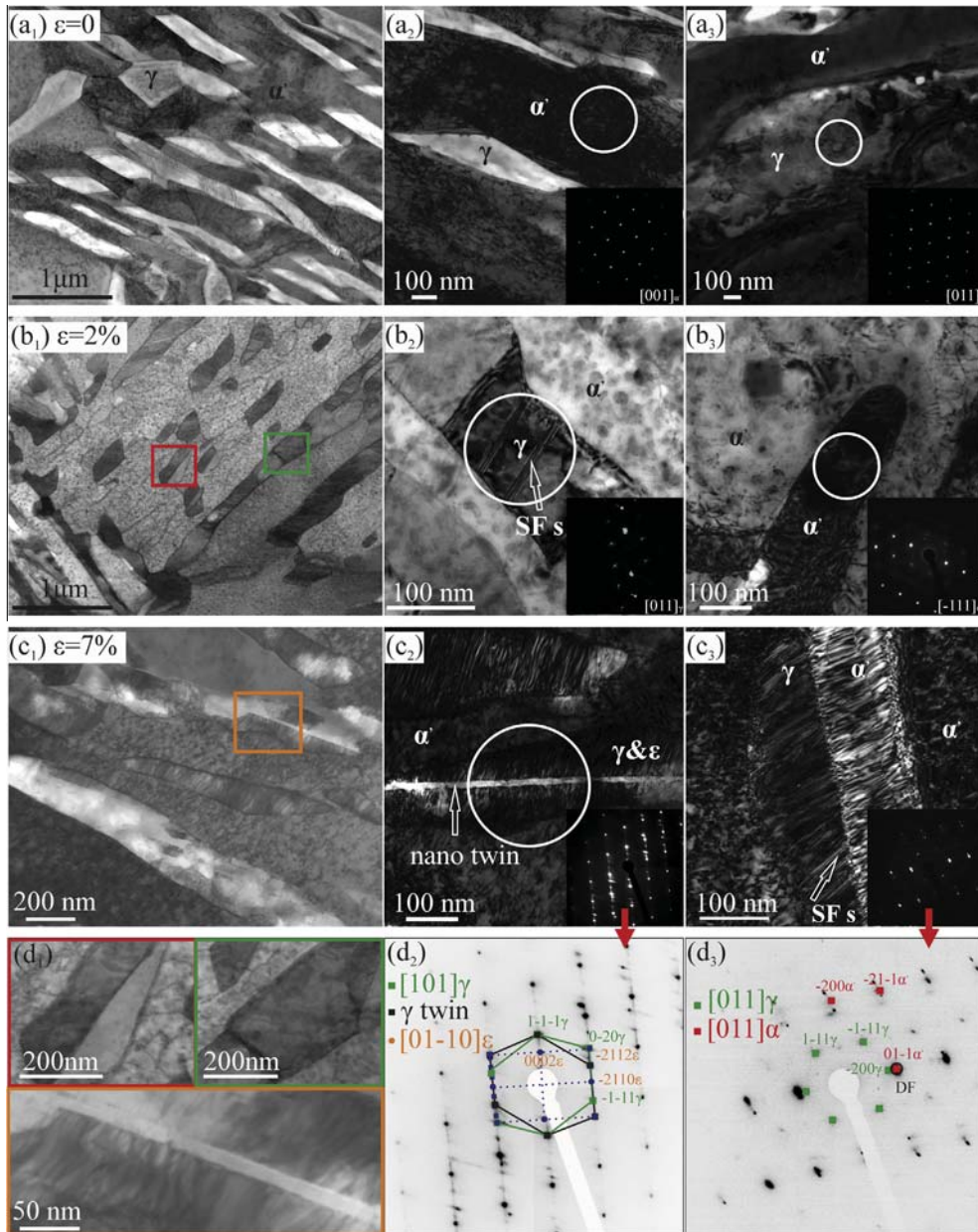
Fig. 7. TEM observation of deformation mechanisms and phase transformation behaviors in TRIP-maraging steel: (a) microstructure in the undeformed state; (b) microstructure after 2% deformation; and (c) microstructure after 7% deformation; (d_1) magnified images from b_1 and c_1; (d_2 and d_3) reconstructed diffraction patterns from (c_2) and (c_3), respectively. White circle represents the aperture applied for the corresponding diffraction.

another γ_{RN} grain, which is again divided into two sub-grains by mechanical twinning, is presented in Fig. 7c$_3$. As revealed by selected-area diffraction, the right portion of this grain (appearing in bright contrast) corresponds to α' martensite. It inherits the SFs from the preceding deformed structure of the parent γ_{RN} sub-grain. The left portion of this γ_{RN} grain, on the other hand, contains a high density of SFs due to deformation and still prevails as an untransformed γ_{RN} grain (Fig. 7d$_3$).

These observations thus demonstrate that for larger γ_{RN} grains plastic strain is accommodated in a coupled manner. First, nanotwins are formed and these twin boundaries divide the γ_{RN} grains into sub-grains. Next, these sub-grains

are deformed to slightly different local strain levels, and only at larger loads does partial transformation to α' martensite occur in a sequential manner. In other words, deformation-induced transformation in larger γ_{RN} grains is observed to be delayed by prior deformation-induced twinning.

These nanotwins, which seem to cause the unexpected transformation size effects, cannot be observed by *in-situ* HR-EBSD due to the limited resolution. Thus an alternative *in-situ* method with higher resolution is applied to track the development of the nanotwins during deformation. More specifically, the appearance of newly formed internal boundaries is captured *in-situ* using secondary

electron and/or electron channeling contrast imaging (ECCI) [43–45], as shown in Fig. 8a and b. These analyses are carried out on the tension side of a three-point bending sample as shown by the schematic sketch in Fig. 8a and b.

As known from the EBSD measurements in Fig. 2, the microstructure is complex even prior to deformation. With straining, microstructure mapping by changing electron channeling conditions becomes difficult due to crystal rotations (Fig. 8b), and shadowing due to surface roughening (Fig. 8a). However, the gradual development of straight boundary segments with abutting grains that appear with different channeling contrasts are clearly observed in the larger γ_{RN} grains with increasing deformation. This is shown in the sequence of Fig. 8b$_1$ (0% strain), b$_2$ (1% strain) and b$_3$ (4% strain) as indicated by the red arrows. Moreover, the morphology of these boundaries is similar to those in Fig. 7b$_1$ and c$_1$. Hence, the observed nanotwinning mechanism found by TEM analysis is further confirmed by the *in-situ* three-point bending experiments.

Besides γ_{RN} and α' martensite, a small amount of ε-martensite, i.e. $\sim$3 vol.%, is also present in the microstructure prior to deformation (Fig. 5). Upon straining to 6.2%, γ_{RN} grains are directly transformed to α' martensite phase. Only a few γ_{RN} grains ($\sim$1 vol.%) transform first to ε-martensite. Of these γ_{RN} grains, only 0.7% transform further to α' martensite phase. This indicates a high resistance of the mechanically induced ε-martensite to further transformation. These phenomena are captured by EBSD, as shown for a representative region in Fig. 9a, cropped from Fig. 4. Here, the γ_{RN} grain marked by the white open arrow transforms spontaneously into α' martensite at 2.3% strain. The majority of the γ_{RN} grains are observed to transform in this manner. The γ_{RN} grain highlighted by the white solid arrow, on the other hand, transforms first to ε-martensite at a strain of 5.0%. This grain prevails as ε-martensite up to a strain of 16.0% and does not transform further.

The synchrotron X-ray diffraction measurements also support the observation of the high mechanical stability of ε-martensite. Peak profiles of samples aged at 600 °C for 8, 4 and 1 h are given for different local strain levels in Fig. 9b$_1$–b$_3$, respectively. For each condition, the 2θ angular regime corresponding to ε-martensite (highlighted in pink) is magnified on the right-hand side. For all aging conditions the ε-martensite intensity varies only within experimental scatter.

4. Discussion

The aim of this study is to investigate the size effects on mechanically induced phase transformations in a systematic manner. We designed a model microstructure with support from DICTRA simulations to provide an optimal γ_{RN} grain size distribution. It is essential in the current approach that all the γ_{RN} grains have the same chemical composition, and hence the same thermodynamic stability. Thus, the observed effects are due to grain size and neighborhood effects but independent of chemical composition. In our discussion of the observed unexpected size dependence of the transformation we follow the sketch shown in Fig. 10.

In the undeformed state, all γ_{RN} grains have a low density of SFs and exhibit a uniform in-grain orientation spread (Figs. 2d, 7a$_1$). Before transformation, the γ_{RN} grains of all sizes are first plastically deformed. They accumulate partial dislocations and regular arrays of SFs (Fig. 7b$_2$). Further deformation leads to massive multiplication of SFs (Fig. 7c$_2$). It was originally proposed by Jaswon [46] that face-centered cubic (fcc) Shockley partial dislocations dissociate to produce faults creating a bcc-related structure. It was reported by Olson and Cohen [47] that from this faulted structure, atoms can shift into bcc positions through a second shear mechanism. Thus, the SFs, particularly those configurations where SF
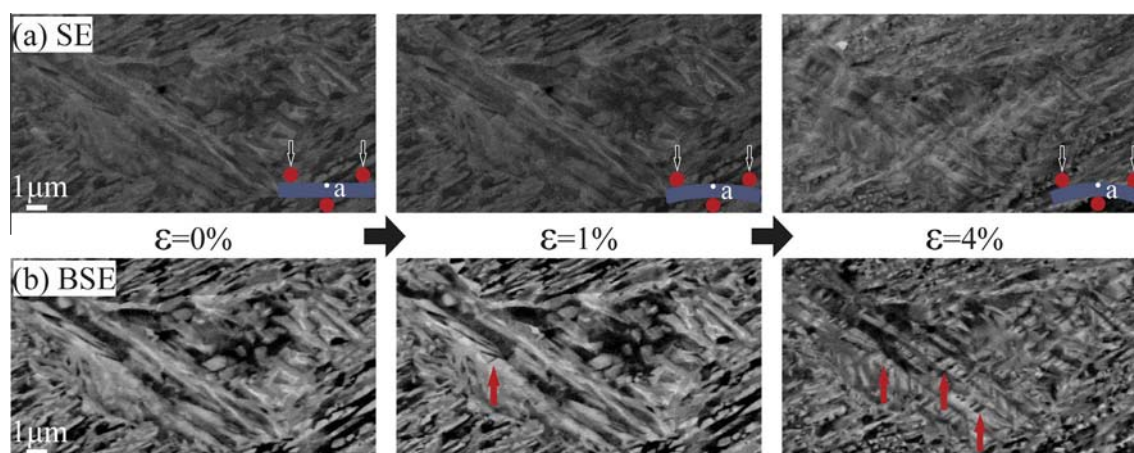

Fig. 8. Investigation of the tension side of a sample during *in-situ* three-point bending experiments by (a) secondary electron imaging, demonstrating the evolving surface morphology; and (b) electron channeling contrast imaging (ECCI), demonstrating the appearance of twin boundaries, as indicated by red arrows. (For interpretation of the references to color in this figure legend, the reader is referred to the web version of this article.)
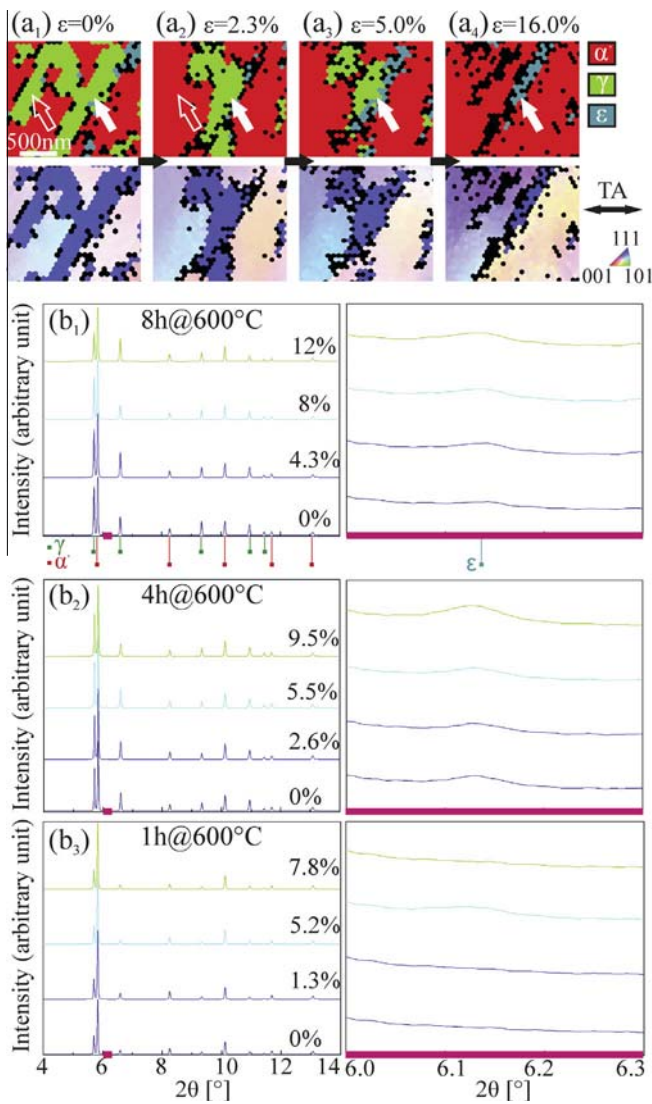
Fig. 9. (Color online) ε-martensite formation analyzed by (a) EBSD phase map and IPF map with respect to the tensile axis (TA) in the 600 °C, 8 h sample, and (b) synchrotron X-ray diffraction measurements of the 600 °C, 8/4/1 h samples with different strain values. ε-martensite diffraction peaks are not indexed together with γ_{RN} phase and α' martensite phase in the left part of (b) due to their relatively low intensities. Instead, one 2θ angular regime (highlighted in pink) corresponding to ε-martensite is magnified and shown on the right part of (b). (For interpretation of the references to color in this figure legend, the reader is referred to the web version of this article.)

intersect each other, may act as potential nuclei for the subsequent α' martensitic transformation (Fig. 7c$_3$). The athermal character of this mechanism is indicated by the fact that the newly formed α' martensite inherits the SFs from the γ_{RN} grains upon transformation (Fig. 7c$_3$).

While this sequence describes the global transformation process observed in this work, a pronounced size effect applies: for the smaller γ_{RN} grains (group I: 0.1–0.3 μm^2), the process described above occurs at small deformations (∼2%) (Fig. 10a$_1$–a$_5$). In the larger γ_{RN} grains (group II: 0.3–4 μm^2) the in-grain deformation proceeds in a more complex way (Fig. 10b$_1$–b$_5$). The formation of SFs is typically accompanied by mechanical twinning. In addition, in

larger grains higher strains are required for the onset of the α' martensite transformation. In the following these points are discussed in more detail.

The build-up of in-grain deformation substructures (partial dislocations, twins) is (i) indirectly indicated by the strongly increasing GAM values observed in the larger γ_{RN} grains (group II), e.g. in Fig. 6b; (ii) directly shown by the TEM analysis in Fig. 7c; and (iii) indicated by the BSE imaging taken during the *in-situ* bending shown in Fig. 8. We found no equivalent indications of such in-grain deformation substructures in the smaller γ_{RN} grains (group I).

Hence, we attribute the transformation size effect essentially to differences in the in-grain deformation substructures evolved in larger and smaller grains, i.e. a TWIP-type deformation behavior is mainly activated in the larger γ_{RN} grains (group II: 0.3–4 μm^2) and is less prevalent in smaller γ_{RN} grains (group I: 0.1–0.3 μm^2).

This size effect associated with mechanical twinning as described herein is consistent with earlier findings [48,49]. The model of Mahajan and Chin [50] explains that nucleation of deformation twins proceeds when fault pairs stemming from two split dislocations react producing three Shockley partials on adjacent planes. The partials associated with each stacking fault are separated owing to the local force balance of such a configuration in a relaxed state. When supported by stress concentrations occurring at the tips of in-grain dislocation pile-ups, the partial spacing of one of the dislocations is reduced down to several nanometers so that it can glide on the adjacent slip plane. If a third fault pair now reaches one side of such a double stacking fault embryo, the two partials that form the interface of the double-layer fault can combine and move to the next adjacent layer and slip away. This final step thus creates a three-layer stacking fault arrangement. The Shockley partials on one side of the fault form an interface whose Burgers vectors sum to zero, making the interface immobile under the applied stress. This leaves the Shockley partials on the opposite side of the stacking fault free to move away from the interface. The subsequent growth of such newly formed twins proceeds by the co-operative motion of the associated partial dislocations on successive {1 1 1} planes [41,47].

The critical twinning stress in the model of Mahajan and Chin as described above is determined by the force required to reduce the internal partial dislocations of two stacking faults to a spacing of less than several nanometers.

As this critical step must be supported by stress peaks at dislocation pile-ups a higher nominal twinning stress is required for the onset of twinning in smaller grains. The reason for that is that in big grains large dislocation pile-ups can readily form owing to the long mean free path over which they can accumulate. Conversely, in small grains large, respectively dense, dislocation pile-ups can only form under higher loads so that the critical twin nucleation stress requires higher nominal stresses. This marks a size effect in terms of facilitating twin nucleation at small loads in large grains and at higher loads in small grains. This effect
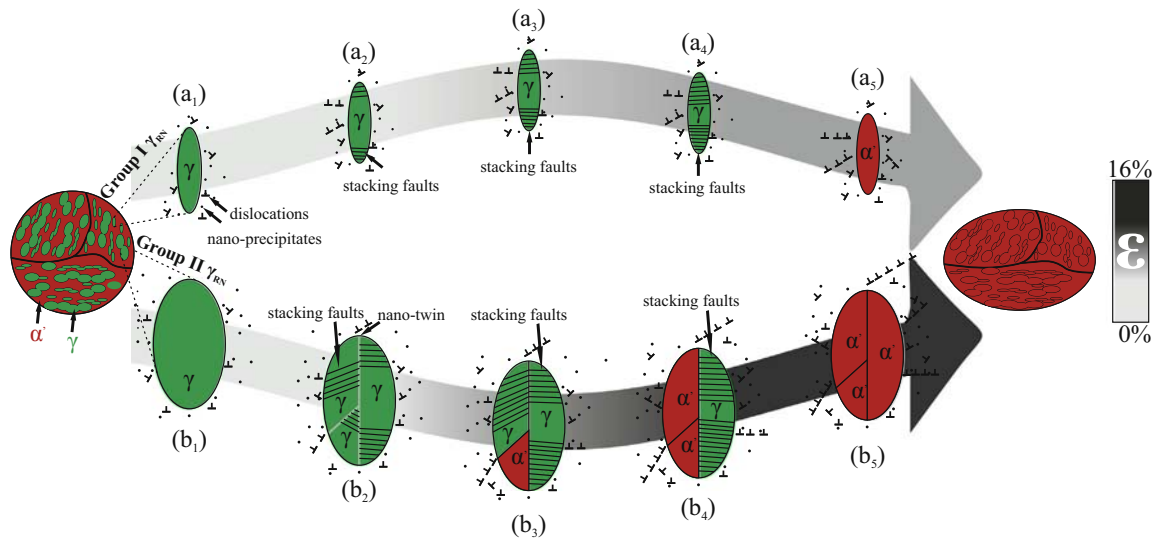
Fig. 10. Schematic sketch of the size-dependent deformation and transformation behaviors in (a) group I (0.1–0.3 μm^2), small γ_{RN} grains; (b) group II (0.3–4 μm^2), larger γ_{RN} grains. All γ_{RN} grains are initially surrounded by α' martensite matrix containing dislocations (T symbols) and nanoprecipitates (dot symbols). The deformation-induced boundaries shown in (b_2) are mechanical twins; α' martensite is nucleated at SFs; SFs are also inherited by the final α' martensite during the athermal phase transformation (not shown here for better visual clarity).

explains the less frequent observation of mechanical twins in the smaller γ_{RN} grains (group I: 0.1–0.3 μm^2).

The increasing GAM values associated with the larger γ_{RN} grains (group II: 0.3–4 μm^2) obtained from the *in-situ* EBSD data indicate the build-up of complex and dense in-grain deformation substructures (Fig. 6b). In addition, the majority of these grains show partial transformation behavior (Fig. 5). Also, we directly observed by TEM analysis that mechanical twins developed in larger grains, dividing them into sub-grains (Fig. 7c1). Each sub-grain develops individual deformation substructure by multiplication of SFs (Fig. 7c2). After sufficient deformation, each compartment eventually transforms to α' martensite (Fig. 7c3). In other words, these grains transform to α' martensite in a stepwise manner and exhibit higher overall mechanical stability. This consecutive effect of in-grain deformation substructures on the phase transformation behavior has been indicated in previous works [51,52]. Leslie et al. [51] demonstrated that the boundaries inside the austenite stabilize it against phase transformation by hindering the growth of the martensite plates. Nakada et al. [52] also reported that twinning influences variant selection of deformation-induced martensite, which may be attributed to the generation of anisotropic strain field because of deformation twinning. In the present work, the Mn content of γ_{RN} is ~16% (Fig. 1), and both TWIP and TRIP act as active deformation mechanisms. High-Mn steels with similar Mn content are also reported to exhibit coexisting TWIP and TRIP effects, though the latter dominates [53]. Combining all these findings, it is proposed that the current chemical composition of γ_{RN} results in a lower threshold for the activation of twinning, e.g. a specific stacking fault energy value related deformation mechanism. In larger γ_{RN} grains, twinning is favored and leads to the build-up of complex and dense in-grain deformation structures. These

deformation twins additionally modify the anisotropy of the strain field of γ_{RN} sub-grains and limit suitable variants of deformation-induced martensite, leading to a delayed overall phase transformation process and higher phase stability in larger γ_{RN} grains.

Another transformation size effect exists for ε-martensite. Previous works described ε-martensite as a transient phase in the γ to α' martensite transformation [54,55]. In these alloy systems, α' martensite was observed to form at intersections of ε-martensite plates. However, in our current work, no intersections of ε-martensite are observed due to the small grain size. The high stability of individual ε-martensite zones is confirmed by the *in-situ* EBSD experiments (Figs. 5 and 8a) and also by the synchrotron X-ray diffraction data (Fig. 8). Hence, we find that small grains (<4.0 μm^2) contain ε-martensite which is stable against further transformation into α' martensite in the current TRIP-maraging steel.

Considering these points, we propose that the γ_{RN} grains in the current TRIP-maraging steel show a size-dependent transformation vs. twinning behavior. The TWIP behavior is mainly activated in larger γ_{RN} grains (group II) and less favored in smaller γ_{RN} grains (group I). In the larger γ_{RN} grains, the mechanical twins and partial dislocation arrays lead to the gradual development of pronounced in-grain deformation substructures. Higher strains are required to initiate the onset of martensitic transformation. Afterwards, these grains completely transform into α' martensite by stepwise transformation of all sub-grains. For smaller γ_{RN} grains, no hint of such a process is observed. Smaller γ_{RN} grains are deformed by multiplication of SFs, and hence phase transformation occurs even at small deformations. Therefore, a coupled size effect of the TWIP and TRIP effects coexists in γ_{RN} grains in the alloy studied here. This leads to the unexpected "smaller is

less stable" phenomenon which can be consistently explained as a transformation size effect. Note that this size effect would also be influenced by various microstructural parameters underlined in the Introduction (crystallographic orientation, chemical composition, neighbouring phases, etc.), and therefore different size effects can be expected in other nanostructured TRIP-assisted steels.

5. Conclusions

The introduction of nanoscale metastable austenite films has been shown to improve the ductility of martensitic steels without sacrificing their strength. Here, the underlying TRIP mechanisms are systematically investigated to better understand these improvements. To this end, we designed a model TRIP-maraging steel microstructure with support from DICTRA simulations. This microstructure allows us to study the mechanical stability of reverted nanoscale austenite (γ_{RN}) due to grain size effects, independent of any influence arising from local chemical composition, the surrounding microstructure or any other microstructural parameters. Through dedicated *in-situ* and *post-mortem* EBSD measurements, an unexpected transformation size effect, i.e. "smaller is less stable", is observed. Follow-up TEM and synchrotron X-ray diffraction analyses reveal that this observation is due to the size-dependent competition between the TWIP and TRIP mechanisms. We attribute the transformation size effect to differences in the evolution of in-grain deformation substructures in larger (group II: 0.3–4 μm^2) and smaller (group I: 0.1–0.3 μm^2) γ_{RN} grains. For larger γ_{RN} grains, mechanical twinning is activated. The development of in-grain deformation substructures stabilizes these grains and results in higher overall mechanical stability. For smaller γ_{RN} grains, mechanical twinning is less favored. Less pronounced in-grain deformation substructures are observed in these grains. Hence, they transform into α' martensite phase even at small deformations. Thus smaller grains exhibit lower stability against transformation. These results also reveal that size effects can be beneficial in alloy design to disperse different deformation mechanisms (e.g. twinning, martensitic transformation) throughout different stages of deformation, thus promoting prolonged resistance to strain localization and failure.

Acknowledgements

References

[1] Fischer FD, Reisner G, Werner E, Tanaka K, Cailletaud G, Antretter T. Int J Plast 2000;16:723.
[2] Zhou Q, Qian L, Tan J, Meng J, Zhang F. Mater Sci Eng A 2013;578:370.
[3] Chiang J, Lawrence B, Boyd JD, Pilkey AK. Mater Sci Eng A 2011;528:4516.
[4] Petrov R, Kestens L, Wasilkowska A, Houbaert Y. Mater Sci Eng A 2007;447:285.
[5] Cao WQ, Wang C, Shi J, Wang MQ, Hui WJ, Dong H. Mater Sci Eng A 2011;528:6661.
[6] Nakada N, Syarif J, Tsuchiyama T, Takaki S. Mater Sci Eng A 2004;374:137.
[7] Wu R, Li W, Zhou S, Zhong Y, Wang L, Jin X. Metall Mater Trans A 2013.
[8] Zhang K, Zhang M, Guo Z, Chen N, Rong Y. Mater Sci Eng A 2011;528:8486.
[9] Raabe D, Ponge D, Dmitrieva O, Sander B. Scr Mater 2009;60:1141.
[10] Dmitrieva O, Ponge D, Inden G, Millán J, Choi P, Sietsma J, et al. Acta Mater 2011;59:364.
[11] Raabe D, Ponge D, Dmitrieva O, Sander B. Adv Eng Mater 2009;11:547.
[12] Yuan L, Ponge D, Wittig J, Choi P, Jiménez JA, Raabe D. Acta Mater 2012;60:2790.
[13] Raabe D, Sandlöbes S, Millán J, Ponge D, Assadi H, Herbig M, et al. Acta Mater 2013;61:6132.
[14] Sugimoto K, Masahiro M. ISIJ Int 1993;33:775.
[15] Xiong XC, Chen B, Huang MX, Wang JF, Wang L. Scr Mater 2013;68:321.
[16] Shi J, Sun X, Wang M, Hui W, Dong H, Cao W. Scr Mater 2010;63:815.
[17] Lee S, Lee S-J, De Cooman BC. Scr Mater 2011;65:225.
[18] Rao BVN, Rashid MS. Metallography 1983;16:19.
[19] Wang XD, Huang BX, Rong YH, Wang L. Mater Sci Eng A 2006;438–440:300.
[20] Ryu JH, Kim D-I, Kim HS, Bhadeshia HKDH, Suh D-W. Scr Mater 2010;63:297.
[21] Park KK, Oh ST, Baeck SM, Kim DI, Han JH, Han HN, et al. Mater Sci Forum 2002;408–412:571.
[22] Yu HY, Kai GY, De Jian M. Mater Sci Eng A 2006;441:331.
[23] Xu Y, Zhang SH, Cheng M, Song HW. Scr Mater 2012;67:771.
[24] Turteltaub S, Suiker ASJ. Int J Solids Struct 2006;43:7322.
[25] Jimenez-Melero E, van Dijk NH, Zhao L, Sietsma J, Offerman SE, Wright JP, et al. Acta Mater 2007;55:6713.
[26] Matsuoka Y, Iwasaki T, Nakada N, Tsuchiyama T, Takaki S. ISIJ Int 2013;53:1224.
[27] García-Junceda A, Capdevila C, Caballero FG, García de Andrés C. Scr Mater 2008;58:134.
[28] Wang P, Xiao N, Lu S, Li D, Li Y. Mater Sci Eng A 2013;586:292.
[29] Jimenez-Melero E, van Dijk NH, Zhao L, Sietsma J, Wright JP, van der Zwaag S. Mater Sci Eng A 2011;528:6407.
[30] Duchateau D, Guitmann M. Acta Metall 1981;29:1291.
[31] Lee S-J, Park K-S. Metall Mater Trans A 2013;44:3423.
[32] Zhang S, Findley KO. Acta Mater 2013;61:1895.
[33] Tirumalasetty GK, van Huis MA, Kwakernaak C, Sietsma J, Sloof WG, Zandbergen HW. Acta Mater 2012;60:1311.
[34] Borgenstam A, Höglund L, Ågren J, Engström A. J Phase Equilib 2000;21:269.
[35] Andersson JO. Calphad 2002;26:273.
[36] Zhao Z, Ramesh M, Raabe D, Cuitiño AM, Radovitzky R. Int J Plast 2008;24:2278.
[37] Raabe D, Sachtleber M, Zhao Z, Roters F, Zaefferer S. Acta Mater 2001;49:3433.
[38] Hammersley AP, Svensson SO, Hanfland M, Fitch AN, Hausermann D. High Press Res 1996;14:235.
[39] Lutterotti L, Matthies S, Wenk H-R. CPD Newslett 1999;21:14.

[40] Morito S, Tanaka H, Konishi R, Furuhara T, Maki T. Acta Mater 2003;51:1789.

[41] Zaefferer S, Wright SI, Raabe D. Metall Mater Trans A 2008;39:374.

[42] Calcagnotto M, Ponge D, Demir E, Raabe D. Mater Sci Eng A 2010;527:2738.

[43] Steinmetz DR, Jäpel T, Wietbrock B, Eisenlohr P, Gutierrez-Urrutia I, Saeed-Akbari A, et al. Acta Mater 2013;61:494.

[44] Gutierrez-Urrutia I, Raabe D. Acta Mater 2011;59:6449.

[45] Gutierrez-Urrutia I, Raabe D. Acta Mater 2012;60:5791.

[46] Jaswon MA. The mechanism of phase transformations in metals. 1956.

[47] Olson GB. Metall Trans A 1976;7A:1905.

[48] Ueji R, Tsuchida N, Terada D, Tsuji N, Tanaka Y, Takemura A, Kunishige K. Scr Mater 2008;59:963.

[49] Gutierrez-Urrutia I, Zaefferer S, Raabe D. Mater Sci Eng A 2010;527:3552.

[50] Mahajan S. Acta Metall 1973;21:1353.

[51] Leslie WC, Miller RL. ASM Trans Q 1964;57:972.

[52] Nakada N, Ito H, Matsuoka Y, Tsuchiyama T, Takaki S. Acta Mater 2010;58:895.

[53] Frommeyer G, Brüx U, Neumann P. ISIJ Int 2003;43:438.

[54] Lee T-H, Shin E, Oh C-S, Ha H-Y, Kim S-J. Acta Mater 2010;58:3173.

[55] Kwon KH, Suh B-C, Baik S-I, Kim Y-W, Choi J-K, Kim NJ. Sci Technol Adv Mater 2013;14:014204.